Mesoporous $Li_4Ti_5O_{12}$ nanoclusters anchored on super-aligned carbon nanotubes as high performance electrodes for lithium ion batteries

Li Sun[1,2], Weibang Kong[2], Hengcai Wu[2], Yang Wu[2], Datao Wang[2], Fei Zhao[2], Kaili Jiang[2,3], Qunqing Li[2,3], Jiaping Wang[2,3*], and Shoushan Fan[2]

1. Beijing Key Laboratory of Materials Utilization of Nonmetallic Minerals and Solid Wastes, National Laboratory of Mineral Materials, School of Materials Sciences and Technology, China University of Geosciences (Beijing), Beijing, China
2. Department of Physics and Tsinghua-Foxconn Nanotechnology Research Center, Tsinghua University, Beijing 100084, China
3. Collaborative Innovation Center of Quantum Matter, Beijing 100084, China
**E-mail: jpwang@tsinghua.edu.cn*

Mesoporous lithium titanate (LTO) nanoclusters are in-situ synthesized in the network of super aligned carbon nanotubes (SACNTs) via a solution-based method followed by heat treatment in air. In the LTO-CNT composite, SACNTs not only serve as the skeleton to support a binder-free electrode, but also render the composite with high conductivity, flexibility, and mechanical strength. The homogeneously dispersed LTO nanoclusters among the SACNTs allow each LTO grain to effectively access the electrolyte and the conductive network, benefiting both ion and electron transport. By the incorporation of LTO into CNT network, mechanical reinforcement is also achieved. When serving as a negative electrode for lithium ion batteries, such robust composite-network architecture provides the electrodes with effective charge transport and structural integrity, leading to high-performance flexible electrodes with high capacity, high rate capability, and excellent cycling stability.

Introduction

Recently many efforts have been made to develop flexible and lightweight energy-storage systems for multifunctional portable/wearable electronic devices, rollup displays, and other smart applications.[1, 2] To develop electrodes in lithium ion batteries (LIBs) with both high energy/power density and high flexibility is the key to their successful application in next-generation electronic devices. Current commercial electrodes suffer from limited mechanical property and high weight percentage of inert components.[3, 4] For example, the widely used metallic current collectors (Cu and Al foil) that provide mechanical support to the electrode possess heavy weight, which accounts for 10~15% of the total weight of a cell and reduces the gravimetric capacity of the whole battery system.[1] Besides, the limited flexibility of the metallic foils causes the active materials to detach easily during deformation and leads to degradation of mechanical and electrochemical performance of the electrode. Binders, which are used to provide mechanical connections between active materials and current collectors in traditional slurry-casted electrodes, also limit the electrochemical performance of the electrode. The insulating binders decrease the conductivity of the electrode, hinder the lithium ion exchange between active materials and the electrolyte, and their electrochemically inactivity also reduces the overall energy density of the electrode.

To address these problems, much work has been done to explore flexible counterparts for these inert components in LIBs. For example, flexible substrates, represented by paper[4], textiles[5] and plastics[6] were extensively studied to replace metallic substrates and provide improved flexibility. However, the conductivities of these substrates were far from satisfactory, and negligible amount of inert components were still involved in the electrodes. Conductive current collectors based on graphene[7] or CNT films[8] were then proposed to provide light weight, high conductivity, high flexibility and efficient wetting between the slurries and the substrates. While in these electrode structures, the insulating binders were still necessary in order to construct an integral electrode, which accounted for an innegligible weight of the electrode. Therefore, the use of flexible carboneous materials (carbon nanofibers, carbon nanotubes and graphene) as both electrode skeleton and charge collector to construct simplified, lightweight electrodes has attracted great interest in order to eliminate traditional metallic current collectors and binders, provide high flexibility and obtain enhanced electrochemical performance.[1] Of all the carboneous materials, the super aligned carbon nanotubes (SACNTs) stand out as a promising material to function as both mechanical skeleton and conductive network to construct flexible, binder-free and current collector-free electrodes.[9-14] The large aspect ratio (~ 10), clean surface, and strong van der Waals force among tubes and bundles in SACNTs allows them to easily entangle into a continuous and robust three-dimensional network, which has been proved as efficient mechanical support for active materials.

Lithium titanate ($Li_4Ti_5O_{12}$, LTO) is a very promising electrode material as it offers the attractive advantages of zero strain, high operating voltage (1.55 V vs. Li/Li^+) and fast lithium ion mobility, which contribute to the excellent reversibility, high structural stability, improved safety and potential high-rate LIB applications. Like other electrode materials, practical applications of LTO are restricted by the low electronic conductivity and lithium diffusion coefficient.[15-17] To overcome these limitations, various nanostructured LTOs with well-designed morphologies and microstructures have been developed,[18,19] of which the mesoporous structures, represented by the mesoporous hollow microspheres,[20] mesoporous LTO nanoclusters,[21] etc., are considered of great potential due to the high specific surface area, high electrode/electrolyte contact area, shortened ion/electron diffusion paths and enhanced intercalation kinetics. Apart from constructing various LTO nanostructures, introduction of carboneous materials, such as CNTs[22-26] and graphene,[27, 28] into LTO is another method that further provides well-extended 3D electron pathways and enhanced rate capability. Some effort has been done to combine mesoporous LTO nanostructures with carboneous materials, represented by the mesoporous LTO single crystals grown on rGO,[27] which was proved to be a promising approach to improve the rate capability. However, in this structure, traditional slurry-coating method was still needed to construct the battery, which limited the mechanical performance of the electrode.

Herein, we report a high-performance, flexible, binder-free and current collector-free electrode based on composited networks of SACNTs and mesoporous lithium titanate. With mesoporous LTO nanoclusters in-situ synthesized in a 3D continuous SACNT network, a highly robust and flexible freestanding composite electrode was obtained. The unique network structure provides critical features required for high-performance electrode, including: 1) efficient electron transport offered by the SACNT network and lithium diffusion promoted by the nanoscale LTO clusters; 2) the interconnected channels offered by the mesoporous LTO nanoclusters for effective ion transport, and 3) the interpenetrating network of SACNTs and LTO nanoclusters, which synergistically provides excellent mechanical robustness and high-rate lithium storage performance. When used as a binder-free anode for LIBs, the LTO-CNT composite exhibited an excellent rate capability with reversible capacities of 164.9 and 164.3 mAh g^{-1} at 10 C and 20 C, respectively, and an outstanding cycling performance with capacity retention of 89% in 1200 cycles at 1 C. Moreover, the electrode presented high flexibility large mechanical strength, demonstrating its potential applications in flexible electronics.

Results and Discussions

The LTO@CNT-400 composite was synthesized by a facile solution-based method[21] followed by low temperature calcination in air. As illustrated in Fig. 1, SACNTs were first dispersed homogenously in the solution of lithium hydroxide under ultrasonication, and then tetrabutyl titanate (TBOT)-ethanol solution was added dropwise under intensive stirring, during which LTO precursors were in-situ formed among the CNT network. Subsequent solvent removal condensed the dispersant into a highly robust and free-standing LTO precursor-CNT film. Note that SACNTs with high aspect ratio and strong interior interactions were necessary for the formation of the binder-free and self-supported film structure.[12, 29] SACNTs acted as both conductive network and mechanical skeleton to load the in-situ grown LTO precursors and entangle them into a composite film. Besides, the following calcination for LTO crystallization was carried out at a relatively low temperature of 400°C in air, which brought little destruction to the SACNT skeleton and resulted in an integrated LTO@CNT-400 composite film. A typical LTO@CNT400 composite film presented average thickness of 55 μm and weight of 4.2 mg/cm^2. High flexibility and apparent homogeneity (Fig. S1a and 1b) was exhibited in the composite, implying a robust structure. As a contrast, the LTO400-CNT$_{mix}$ composite, prepared by simply dispersing LTO400 and CNTs in solution followed by deposition, turned out to be rough with many visible white LTO powders on the surface (Fig. S1c) and could be easily teared out, revealing poor attachment of its components.

The apparent homogeneity and high mechanical strength of the LTO@CNT400 composite was further supported by its robust microstructure via TEM and SEM investigation. Fig. 2a shows the SEM image of the LTO precursor-CNT mixture, in which LTO precursors were well supported by the 3D continuous CNT framework. Such framework provided abundant adsorption points, favoring LTO crystallization and alleviating its aggregation, leading to an inseperate complex of LTO and CNTs after calcination. As shown in Fig. 2b, in the LTO@CNT-400 composite, clusters of LTO embedded homogeneously in the CNT network, with CNTs penetrating throughout the LTO clusters, ensuring direct interfacial contact for effective electron transport. At the same time, abundant pores existed in the interconnected channels, which allowed easy electrolyte infiltration for fast ion exchange. The EDX elemental analysis revealed presence of Ti, O and C in the sample, and elemental map of Ti (inset of Fig. 2b) further confirmed the homogeneous distribution of LTO.

Detailed structures of the composite were shown in Fig. 2c, in which LTO nanoclusters (size: 50~100 nm) anchored uniformly among the CNT network. The TEM image at higher magnification (Fig. 2d) revealed the intertwining structure between LTO and CNTs. Similar to those synthesized in absence of CNTs,[21] the LTO nanoclusters here consisted of densely packed and interconnected LTO grains of a few nanometers. Nano-sized pores (marked by the red circles) were observed within the nanoclusters, which benefited electrolyte infiltration and lithium transportation. A magnified image in Fig. 2e showed distorted carbon rings and chopped tubes as marked by the white arrows, which might be caused by the heat treatment in air and the complex chemical reactions when forming LTO. Clear grain lattice can be found in the HRTEM image shown in Fig. 2f, with interlayer spacing of 0.48 nm, consistent to the (111) plane in crystalline LTO, revealing the well-crystallized feature of LTO.

The microstructures presented here implied the efficiency of the facile in-situ synthesis process in achieving integrated and homogeneous composite structures. On one hand, the in-situ generation of LTO nanoclusters suppressed the agglomeration of CNTs, leading to 3D extended electron pathways. On the other hand, CNTs as a support material provided abundant adsorption points, inducing nucleation, growth and formation of fine LTO nanostructures with uniform dispersion. In comparison, rather inhomogeneous microstructure was found in the LTO400-CNT$_{mix}$ sample with large LTO aggregates floated on top of SACNTs. Besides, the calcining temperature was also important to control the LTO microstructures. When the temperature was raised to 800 ^{o}C, non-porous LTO grains of 100~200 nm were formed, which exhibited weakened contact with the SACNT network (Fig. S2a) and large aggregates were found in the SEM images (Fig. S2b).

The XRD pattern of the LTO@CNT-400 composite (Fig. 3a) exhibited a clear peak at around 26°corresponding to the (002) plane of CNTs. All the other peaks consisted with those of $Li_4Ti_5O_{12}$ (PDF#72-0426) plotted by the red column lines. Compared to the sharp peaks in LTO@CNT-800 (Fig. S3a), all peaks in LTO@CNT-400 presented a broadening effect, indicating the smaller grain size. Through the (400) plane at 43.2^{o}, the average grain size was calculated as 5.06 nm based on the Scherrer's equation, in good accordance with those observed in the TEM images. The thermogravimetric analysis (TGA) in Fig. 3b revealed a LTO percentage of 77.5 wt% in the composite. It should be mentioned that composites with even larger LTO content of about 90% were prepared. However, the insufficient CNTs in the composite induced low electronic conductivity and consequently inferior electrochemical performance of the electrode. The Raman spectra of the LTO@CNT-400 composite (Fig. 3c) exhibited three characteristic bands of CNTs, i.e., the D band at about 1332 cm^{-1}, G band at about 1585 cm^{-1}, and D' band at about 1617 cm^{-1}, while the I_D/I_G ratio increases from 0.82 in pristine CNTs to 1.25 in the LTO@CNT-400 composite, indicating higher defect concentration in the heat treated CNTs. These defects agreed well with the distorted tubes observed in Fig. 2e, which were created during the heat treatment in air and the complex chemical reactions when forming LTO. In addition to the characteristic bonds of CNTs, typical bonds of LTO were also observed in 100~1000 cm^{-1}.[26]

Stress-strain curves of pristine CNT and the LTO-CNT composites are given in Fig. 4a. Pristine CNT films delivered a strength of 0.46 MPa and a fracture strain of 4.47%. Incorporation of LTO into CNT created an intertwined structure between both components, resulting in mechanical reinforcement in LTO@CNT-400 and LTO@CNT-800. The largest strength of 1.90 MPa and fracture strain of 13.34% were achieved in LTO@CNT-400, followed by smaller values (0.97 MPa, 10.10%) in LTO@CNT-800 with larger LTO grains and non-porous structures. As supposed, the LTO400-CNT$_{mi}$ exhibited the smallest strength of 0.09 MPa and fracture strain of 2.76% due to the inhomogeneous microstructure and the poor interaction between CNTs and LTO, further confirming the necessity of the in-situ synthesis process in obtaining a composite with high mechanical integrity. Both the high strength and high flexibility are beneficial for possible application in flexible devices.

Brunauere Emmette Teller (BET) measurements further confirmed the porous microstructure of the LTO@CNT-400 composite. The composite exhibited a large BET surface area of 224.37 m^2/g and cumulative pore volume of 0.648 cm^3/g. The nitrogen adsorption-desorption isotherm curve in Fig. 4b was sorted into type IV according to the IUPAC classification, with an distinctive hysteresis in th relative pressure (P/P$_0$) range of 0.4~1.0, which can be attributed to the mesopores in the porous stacking of $Li_4Ti_5O_{12}$ particles. The corresponding Barrette Joynere Halenda (BJH) desorption po size distribution (the inset of Fig. 4b) showed two peaks at 3.3 nm and 8.9 nm, possibly corresponding to the pores within LTO clusters[21] and the pores between CNTs and LTO. In comparison, the N adsorption-desorption curve of the LTO@CNT-800 composite presented no hysteresis (Fig. S3b), implying absence of mesopores. The mesoporous structures revealed in LTO@CNT-400 agreed well with that observed in TEM, which was expected to improve the electrolyte infiltration and consequently facilitate the lithium ion transfer and high-rate performance.

With rational design of the LTO nanoclusters well embedded in flexible SACNT skeleton, the high-rate performance of the LTO@CNT-400 composite is dramatically facilitated. The cyclic voltammogram (CV) curves of the LTO@CNT-400 composite are shown in Fig. 5a at the scanning rates of 0.1~2 mV/s in the range of 1~2.5 V. Each of the CV curves exhibited a couple of sharp redox peaks, corresponding to the characteristic peaks of Li^+ insertion/extraction in spinel LTO. Moreover, the peaks remained stable and sharp even at a high scanning rate of 2 mV/s, indicating a fast Li^+ insertion/extraction process, which was beneficial for its high rate capability. As shown in Fig. 5b, with the current densities varied from 0.5C to 20 C, the discharge capacities of the LTO@CNT-400 composite remained stable with little degradation. The capacities at 0.5C, 1C, 2C, 5C, 10C and 20C were 173.9~170.6, 170.3~168.7, 167.1~166.3, 166.2~165.1, 164.9~164.7 and 164.3~159.9 mAh g^{-1}, respectively. Even at the rate as high as 50C, the LTO@CNT-400 still exhibited remarkable capacities of 104.4~103.6 mAh g^{-1}, corresponding to 60% of that at 0.5C. Furthermore, when the discharge current reduced back to 0.5C and 0.2C in sequence, high capacities of 170.7 and 167.2 mAh g^{-1} were recovered with no significant decline, demonstrating the good reversibility of the electrode. While for the case of LTO@CNT-800, although comparable capacities of 171.9~167.1 and 166.3~164.3 mAh g^{-1} were achieved at smaller rates of 0.5C and 1C, larger capacity degradation was present as the rate was raised further. For example, capacities of 158.3~157.2, 146.4~146.7, 129.9~130.2, 78.4~72.8, 50.9~52.4 mAh g^{-1} at rates of 2C, 5C, 10C, 20C, and 50C were obtained in the LTO@CNT-800 composite, corresponding to 94%, 88%, 78%, 47% and 48% of that in LTO@CNT-400. As a contrast, the LTO400-CNT_{mix} composite, showed inferior rate performances with the smallest capacities of 157.8~155.5, 149.1~145.1, 137.1~136.7, 112.4~101.7, 34.5~39.7 and 39.6~30.5 mAh g^{-1} at elevated rates between 0.5C and 50C. The capacities delivered by the LTO400-CNT_{mix} composite electrode were even smaller than the previously reported slurry-casted electrode prepared from bare $Li_4Ti_5O_{12}$

nanoclusters,[21] which generally originated from the rather inhomogeneous composite structure and poor attachment between components in LTO400-CNT$_{mix}$. The great advantage of LTO@CNT-400 in high-rate performance stemmed from the small dimension (50~100 nm) and mesoporous structure of the LTO nanoclusters that reduced lithium ion diffusion length and facilitated electrolyte infiltration and ion transfer, as well as the in-situ formed robust hybrids of LTO and CNTs that offered persistent contacts between LTO grains and CNTs to improve electron transport.

The effect of different LTO/CNT structures on the electrode performances was further probed by the electrochemical impedance spectra (EIS). All the EIS in Fig. 5c presented a typical semicircle attributed to the charge transfer impedance. It was clearly shown that the charge transfer resistance of LTO@CNT-400 was lower than LTO@CNT-800, indicating improved electronic conductivity and lithium ion diffusion. While the LTO400-CNT$_{mix}$ showed much higher impedance, which suggested that the in-situ synthesized LTO directly grown on SACNT network was favorable for fast electron transport. The better reaction kinetics revealed by the EIS of LTO@CNT-400 was responsible for the improved rate performance.

The excellent rate performance of LTO@CNT-400 composite can be attributed to the synergistic effects of mesoporous LTO nanoclusters and the 3D conductive SACNT network. As illustrated in Fig. 5d, compared to LTO@CNT-800 with non-porous LTO grains (100~200 nm), the LTO@CNT-400 offers super tiny LTO grains in the clusters, each of which can keep close contact to the SACNTs penetrated through them, therefore shortening the electron diffusion length and improving the conductivity of the electrode. Besides, the mesoporous structure of the LTO nanoclusters favors the infiltration of the electrolyte, which contributes to the shortened ion transfer pathways and highly efficient Li^+ exchange.

Apart from the high rate performance, the cycling performance of the composites was tested. As shown in Fig. 6a, the LTO@CNT-400 anode exhibited an initial discharge capacity of 173.7 mAh g^{-1} at 1C, while the LTO@CNT-800 anode delivered compatible initial capacity of 169.7 mAh g^{-1} (Fig. S4a). However, the cycling stability was significantly different (Fig. S4b). The LTO@CNT-400 cathode exhibited favorable cyclibility with nearly 95.3% of capacity retention (165.5 mAh g^{-1}) after 400 cycles, while the capacity of LTO@CNT-800 decayed to around 150.3 mAh g^{-1} after 400 cycles, with cyclic degradation rate of 88.5%. Similarly to the rate test, the smallest capacities of 149~118 mAh g^{-1} in 400 cycles were obtained in the LTO400-CNT$_{mix}$ composite. Compared to the slope profiles of the potential-capacity relationship in LTO@CNT-800 and LTO400-CNT$_{mix}$, the LTO@CNT-400 anode exhibited long and flat plateaus both in the 1st and 400th cycles, indicating favorable electrochemical kinetics (Fig. S4b). Furthermore, the long-term cycling behaviors of the LTO@CNT-400 composites were also tested at 5C and 10C. As shown in Fig. 6a, a reasonably high capacity of 154.7 mAh g^{-1} was exhibited even after 1200 cycles, corresponding to the capacity retention of 89%, implying extremely favorable electrochemical processes. Moreover, when the current density increased to 5C and 10C, extraordinary cycling performance was still exhibited, with impressive capacities of 168.2~130.8 mAh g^{-1} and 134.3~85.3 mAh g^{-1} in 1200 charge/discharge cycles, corresponding to capacity retention as high as 77.8% and 63.5%. Apart from the high capacities, the high coulombic efficiency of the LTO@CNT-400 composite maintained around 100% during 1000-cycle long-term cycling, demonstrating the high reversibility and efficiency. These excellent cycling performances were attributed to the homogeneous distribution of both electrode components as well as the structural robustness. In addition, as discussed earlier, the mesoporous LTO nanoclusters provided abundant open space to facilitate the active LTO to gain access to both the electrolyte and the conductive SACNTs closely, thus allowing for excellent high-rate performance. The photo of the electrode taken after 1,000 cycles at 1C (the inset of Fig. 6b) showed that the composite remained as integrity with high flexibility. No mechanical cracks or destruction were found in the composite. Additionally, no large LTO aggregates were found in the SEM image (Fig. 6b) of the cycled electrode, further confirming the persistently dispersed LTO during cycling.

The electrochemical performance demonstrated here is among the best results in LTO-CNT composites reported up to now. For example, earlier methods to synthesize nano LTO-CNT composites include liquid phase deposition,[24] in-situ growth of LTO on CNTs[17] and in-situ growth of CNTs on LTO,[23] etc., while the relative small interactions within CNTs used in these methods cannot support a binder-free electrode. As a result, additional binders, carbon black and current collectors were involved in these methods, limiting their applications in flexible electronics. Very recently, a binder-free and flexible nanostructured LTO/CNT composite was synthesized.[26] Though a capacity of around 110 mAh g^{-1} were demonstrated at 50 C, slightly higher than that of around 104 mAh g^{-1} in LTO@CNT-400, the capacities at other current densities were comparable or even larger in LTO@CNT-400. Besides, long-term cycling performance of in LTO@CNT-400 was also of great advantage. Capacities of 173.7~154.7 mAh g^{-1} at 1C in 1200 cycles were delivered in LTO@CNT-400, while in their work smaller capacities around 105 mAh g^{-1} were obtained at smaller current density of 1 A g^{-1} (0.58C) in long-term cycling tests. The superiority of the LTO@CNT-400 could be attributed to the combination of mesoporous LTO nanoclusters and the highly flexible and conductive SACNTs. Due to the relatively large inter-grain spacing in the LTO clusters, the whole LTO materials including those in the interior position can gain sufficient access to the electrolyte, effectively fascinating the lithium ion transportation at high charge-discharge rates. In addition, the CNTs penetrated through the LTO nanoclusters could serve as a fast electron transport channel and could be another reason for the excellent rate performance of the LTO@CNT-400 anode. Moreover, the self-supported LTO@CNT-400 structure not only avoided the extra weight of binders and current collectors, but also prevented the agglomeration of active materials during cycling, resulting in further enhanced cycle stability. Besides, the synthesis method in this work was rather simple including facile solution-based method and low-temperature heat treatment in air, which is considered a reservation of energy.

Conclusions

A flexible and binder-free LTO@CNT-400 composite was fabricated, in which super aligned CNTs were employed as the skeleton to load the in-situ fabricated mesoporous LTO nanoclusters. The SACNT network rendered the composites with excellent electrical conductivity and robust framework to support a binder-free electrode with high flexibility and mechanical integrity, while the mesoporous LTO nanoclusters that were in-situ synthesized among the SACNT network provided interconnected porous structures, which ensured the accessibility of active materials to both conductive SACNTs and liquid electrolyte. The special composite structure rendered the composite anode with an ultrahigh capacity of 173.9 mAh g^{-1} at 0.5 C, a favorable high-rate capability of 164.3 mAh g^{-1} at 20 C, and an impressive cycling stability of 89% capacity retention after 1200 cycles at 1 C. The free-standing and binder-free electrode is promising for possible applications in future flexible electronic devices.

Experimental

Material preparation

SACNT arrays with a diameter of 20~30 nm and a height of 300 μm were synthesized on silicon wafers by chemical vapor deposition (CVD), with iron as the catalyst and acetylene as the precursor. Details of the synthesis procedure can be found in previous papers.[13, 30]

LTO-CNT composite electrode was prepared via an in-situ synthesis of LTO nanoclusters[21] reported previously in presence of SACNTs. Typically, 20 mg SACNTs were dispersed in 100 mL ethanol with sonication for 1 h and then 10.23 mg lithium hydroxide (Alfa Aesar, anhydrous, 99.995% purity) was dissolved into 20 mL deionized water and added to the above SACNT suspension to form the base solution. 173.02 mg $TiO(C_4H_9)_4$ (Alfa Aesar, 98% purity) was dissolved in 50 mL ethanol to form a clear solution. When the base solution was heated to 80 ºC, the $TiO(C_4H_9)_4$ solution was added into the base solution and then stirred quickly. An instantaneous formation of white precipitation was generated and anchored onto the SACNTs. The resulted mixture was stirred at 80 ºC to allow completion of the reaction. The resultant mixture was dried at 60 ºC and a LTO precursor-SACNT mixture film was detached from the container. Calcination at 400 ºC in air was conducted to the mixture to allow further crystallization of $Li_4Ti_5O_{12}$ and the LTO@CNT-400 composite was obtained. Heat treatment in Ar at 800 ºC was also performed to the LTO precursor-CNT composite to obtain the control sample, marked as LTO@CNT-800.

To demonstrate the advantage of the in-situ synthesis of LTO, a second control sample that simply mixed SACNTs and LTO-400 synthesized using the same method in absence of CNTs was also prepared. Generally, 20 mg SACNTs and 80 mg LTO-400 was dispersed in 100 mL ethanol/H_2O (3:1) solution. The mixture was then stirred under 80 ºC to allow removal of the solvent and achieve a highly concentrated mixture with optimized homogeneity. Then the mixture was dried at 60 ºC. Similarly, a binder-free film could be detached from the container bottom, marked as $\text{LTO400-CNT}_{\text{mix}}$.

Material Analysis

The crystalline structures were characterized by X-ray diffraction (XRD) using a diffractometer (Rigaku, Cu Kα radiation) in the 2θ range from 10º to 80º. Thermogravimetric analysis (TGA) was conducted on Pyris 1 TGA (Perkin Elmer, USA) at a heating rate of 10 °C min^{-1} in air from 25 to 800 °C. Tensile tests were performed using an Instron 5848 microtester with a strain rate of 1% min^{-1} and a 1 cm gauge length. The microstructure was characterized by scanning electron microscope (SEM, Sirion 200, FEI) and transmission electron microscope (TEM, Tecnai G2F20, FEI). Raman spectroscopy was performed on a Horiba spectrometer with He-Ne laser excitation at 633 nm. The Brunauere Emmette Teller (BET) measurements were performed on a surface area and porosity analyzer (ASAP 2020).

Electrochemical measurement

Coin-type half-cells were assembled in a glove box filled with protective argon gas (M. Braun inert gas systems Co. Ltd., Germany) with the LTO@CNT-400, LTO@CNT-800 and LTO400-CNT$_{mix}$ composite as the working electrodes and pure lithium foil as the reference electrode. A polypropylene film (Celgard 2400) was used to separate the cathode and the anode. 1 M $LiPF_6$ in a 1:1:1 (volume) mixture of ethylene carbonate, dimethylcarbonate and ethylmethyl carbonate as the electrolyte was used as electrolyte. The cycling tests were made on a Land battery test system (Wuhan Land Electronic Co., China) in a voltage window of 1~2.5 V at different charge/discharge rates at room temperature. The rate tests were performed by discharging the electrode at varied charge rates while charged at a constant rate of 0.5 C. The cyclic voltammetry tests and electrochemical impedance spectroscopy (EIS) measurement were performed between 1 V and 2.5 V using a Potentiostat/Galvanostat (EG&G Princeton Applied Research 273A).

Acknowledgements

This work was supported by the National Basic Research Program of China (2012CB932301) an the NSFC (51102146 and 51472141).

Notes and references

1. Zhou, G. M.; Li, F.; Cheng, H. M. *Energy Environ. Sci.* **2014,** 7, (4), 1307-1338.
2. Nishide, H.; Oyaizu, K. *Science* **2008,** 319, (5864), 737-738.
3. Landi, B. J.; Ganter, M. J.; Cress, C. D.; DiLeo, R. A.; Raffaelle, R. P. *Energy Environ. Sci.* **2009,** 2, (6), 638-654.
4. Hu, L. B.; Choi, J. W.; Yang, Y.; Jeong, S.; La Mantia, F.; Cui, L. F.; Cui, Y. *P Natl Acad Sci USA* **2009,** 106, (51), 21490-21494.
5. Liu, Y.; Gorgutsa, S.; Santato, C.; Skorobogatiy, M. *J Electrochem Soc* **2012,** 159, (4), A349-A356.
6. Meng, F. H.; Ding, Y. *Adv Mater* **2011,** 23, (35), 4098-+.
7. Gwon, H.; Kim, H. S.; Lee, K. U.; Seo, D. H.; Park, Y. C.; Lee, Y. S.; Ahn, B. T.; Kang, K. *Energy Environ. Sci.* **2011,** 4, (4) 1277-1283.
8. Wang, K.; Luo, S.; Wu, Y.; He, X. F.; Zhao, F.; Wang, J. P.; Jiang, K. L.; Fan, S. S. *Adv Funct Mater* **2013,** 23, (7), 846-85
9. Wu, Y.; Wang, J. P.; Jiang, K. L.; Fan, S. S. *Front Phys-Beijing* **2014,** 9, (3), 351-369.
10. Luo, S.; Wu, H. C.; Wu, Y.; Jiang, K. L.; Wang, J. P.; Fan, S. S. *J. Power Sources* **2014,** 249, 463-469.
11. He, X. F.; Wu, Y.; Zhao, F.; Wang, J. P.; Jiang, K. L.; Fan, S. S. *J Mater Chem A* **2013,** 1, (37), 11121-11125.
12. Luo, S.; Wang, K.; Wang, J. P.; Jiang, K. L.; Li, Q. Q.; Fan, S. S. *Adv Mater* **2012,** 24, (17), 2294-2298.
13. Jiang, K. L.; Wang, J. P.; Li, Q. Q.; Liu, L. A.; Liu, C. H.; Fan, S. S. *Adv Mater* **2011,** 23, (9), 1154-1161.
14. Sun, L.; Kong, W. B.; Jiang, Y.; Wu, H. C.; Jiang, K. L.; Wang, J. P.; Fan, S. S. *J Mater Chem A* **2015,** 3, (10), 5305-5312.
15. Chen, S.; Xin, Y. L.; Zhou, Y. Y.; Ma, Y. R.; Zhou, H. H.; Qi, L. M. *Energy Environ. Sci.* **2014,** 7, (6), 1924-1930.
16. Zhao, L.; Hu, Y. S.; Li, H.; Wang, Z. X.; Chen, L. Q. *Adv Mater* **2011,** 23, (11), 1385-1388.
17. Shen, L. F.; Uchaker, E.; Zhang, X. G.; Cao, G. Z. *Adv Mater* **2012,** 24, (48), 6502-6506.
18. Shen, L. F.; Yuan, C. Z.; Luo, H. J.; Zhang, X. G.; Xu, K.; Xia, Y. Y. *J Mater Chem* **2010,** 20, (33), 6998-7004.
19. Tang, Y. F.; Yang, L.; Fang, S. H.; Qiu, Z. *Electrochim Acta* **2009,** 54, (26), 6244-6249.
20. Yu, L.; Wu, H. B.; Lou, X. W. *Adv Mater* **2013,** 25, (16), 2296-2300.
21. Sun, L.; Wang, J. P.; Jiang, K. L.; Fan, S. S. *J. Power Sources* **2014,** 248, 265-272.
22. Wang, J. Q.; Li, W. H.; Yang, Z. Z.; Gu, L.; Yu, Y. *Rsc Adv* **2014,** 4, (48), 25220-25226.
23. Shu, J.; Hou, L.; Ma, R.; Shui, M.; Shao, L. Y.; Wang, D. J.; Ren, Y. L.; Zheng, W. D. *Rsc Adv* **2012,** 2, (27), 10306-10309.
24. Ni, H. F.; Fan, L. Z. *J. Power Sources* **2012,** 214, 195-199.
25. Shen, L. F.; Yuan, C. Z.; Luo, H. J.; Zhang, X. G.; Xu, K.; Zhang, F. *J Mater Chem* **2011,** 21, (3), 761-767.
26. Jia, X. L.; Kan, Y. F.; Zhu, X.; Ning, G. Q.; Lu, Y. F.; Wei, F. *Nano Energy* **2014,** 10, 344-352.
27. Chen, W. N.; Jiang, H.; Hu, Y. J.; Dai, Y. H.; Li, C. Z. *Chem Commun* **2014,** 50, (64), 8856-8859.
28. Kong, D. Z.; Ren, W. N.; Luo, Y. S.; Yang, Y. P.; Cheng, C. W. *J Mater Chem A* **2014,** 2, (47), 20221-20230.
29. Sun, L.; Li, M. Y.; Jiang, Y.; Kong, W. B.; Jiang, K. L.; Wang, J. P.; Fan, S. S. *Nano Lett* **2014,** 14, (7), 4044-4049.
30. Jiang, K. L.; Li, Q. Q.; Fan, S. S. *Nature* **2002,** 419, (6909), 801-801.

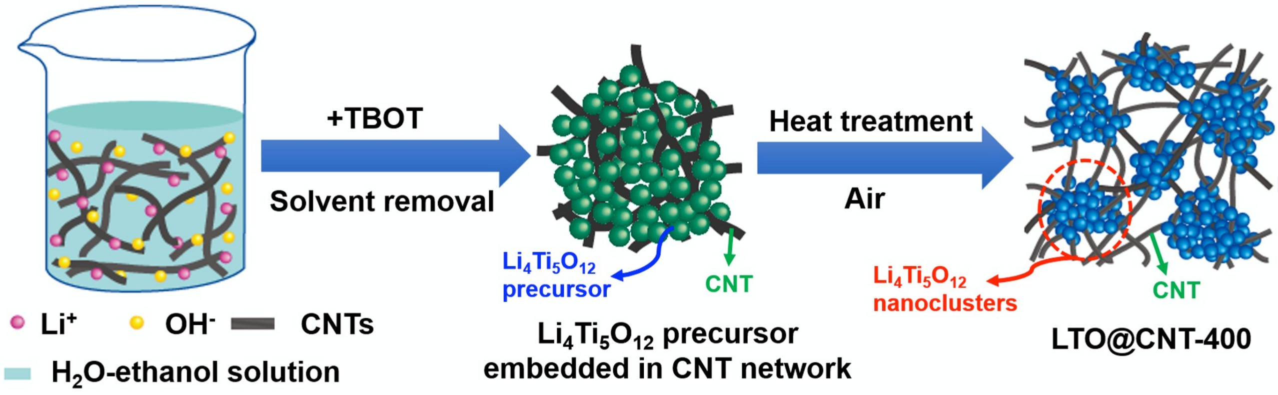

Fig. 1 The synthesis procedure of the LTO@CNT-400 composite.

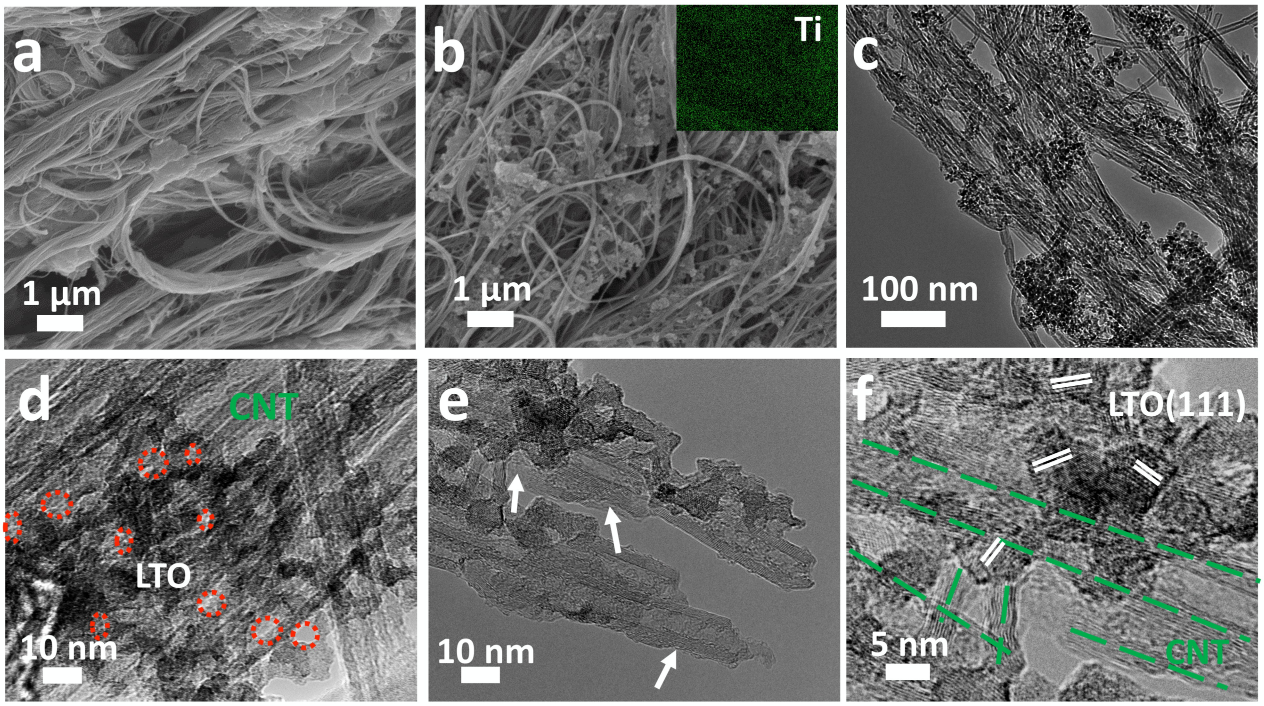

Fig. 2 SEM images of the (a) LTO precursor-CNT mixture and (b) LTO@CNT-400 composite. The inset of (b) gives the EDX elemental map of Ti in (b). (c)TEM and (d, e, f) HRTEM images of the LTO@CNT-400 composite.

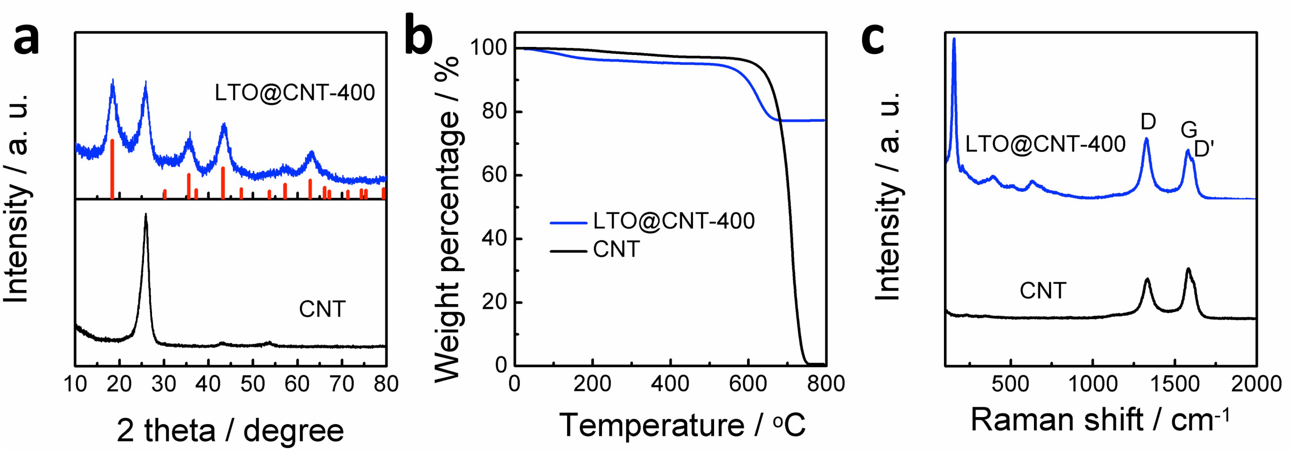

Fig. 3 (a) XRD patterns, (b) TGA curves and (c) Raman spectra of LTO@CNT-400 and CNT.

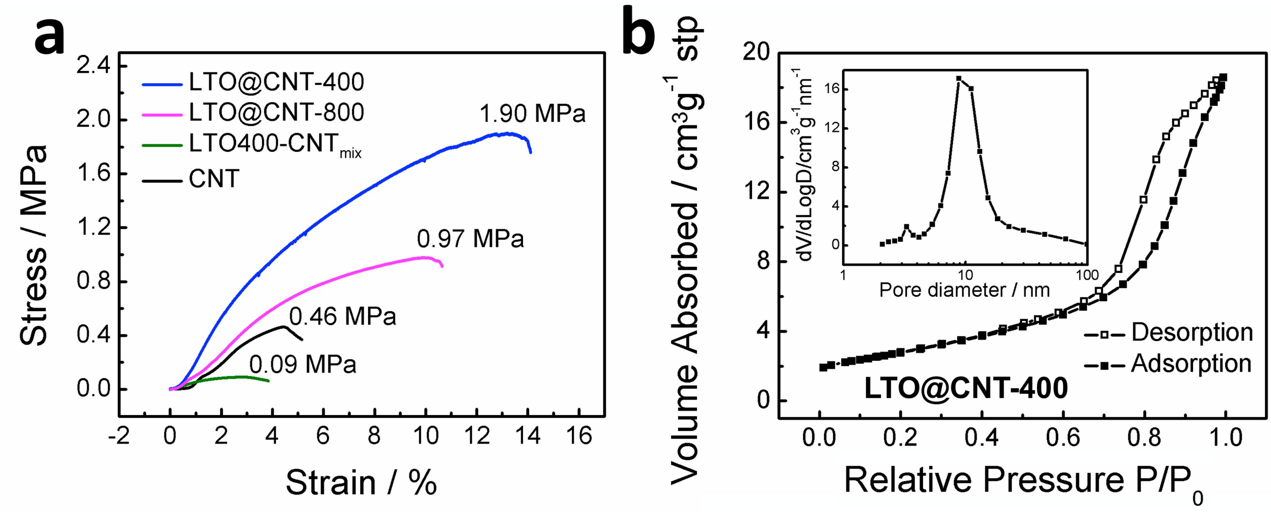

Fig. 4 (a) Stress-strain curves of LTO@CNT-400, LTO@CNT-800, LTO400-CNT$_{mix}$ and CNT. (b) N_2 adsorption-desorption isotherm loop of LTO@CNT-400, with an inset of the pore size distribution.

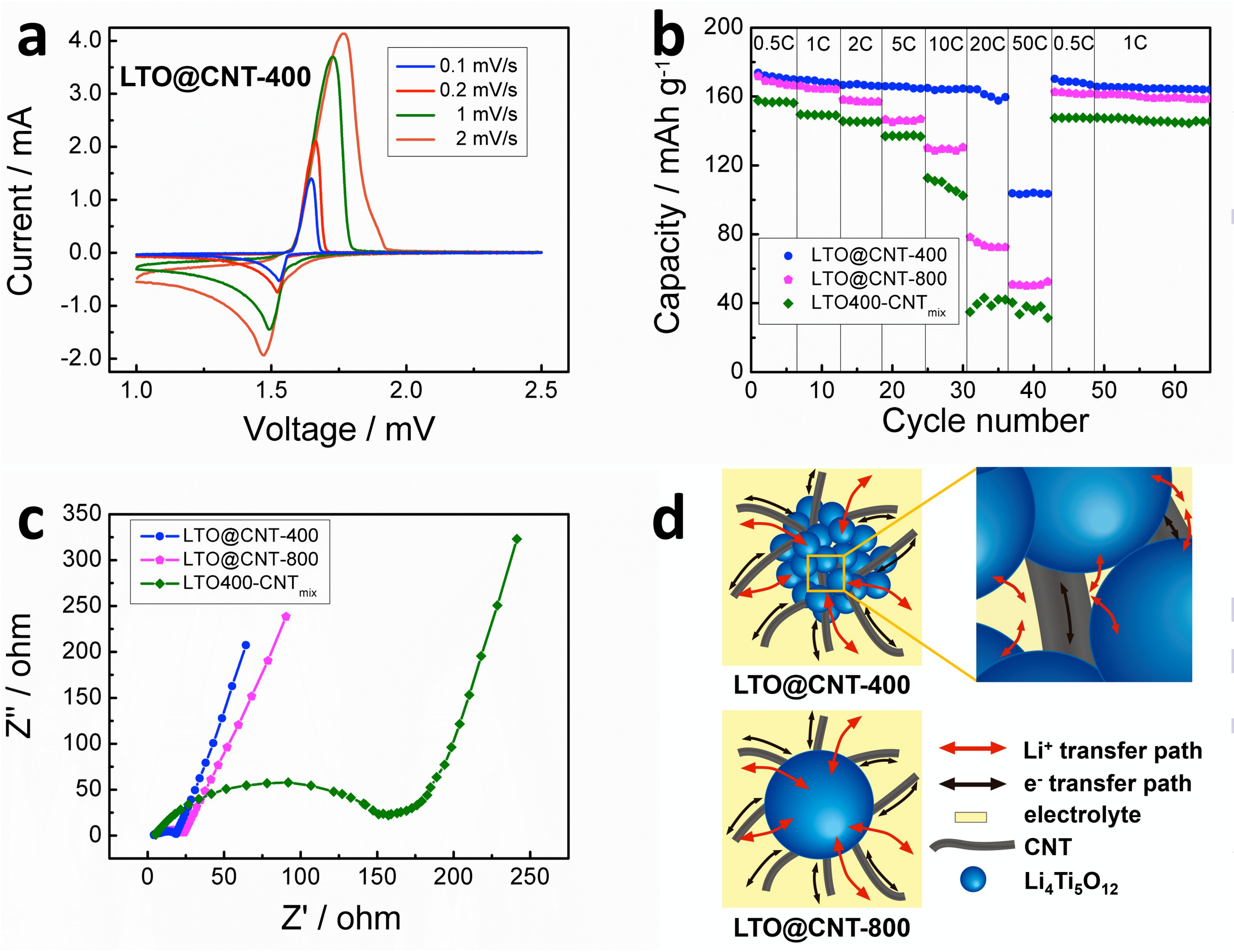

Fig. 5 (a) CV curves of the LTO@CNT-400 composites at the scanning rates of 0.1, 0.2, 1 and 2 mV/s. (b) Rate performance and (c) EIS spectra of the LTO@CNT-400, LTO@CNT-800 and LTO400-CNT$_{mix}$ composites. (d) Illustration of the electron and lithium ion transfer paths in LTO@CNT-400 and LTO@CNT-800.

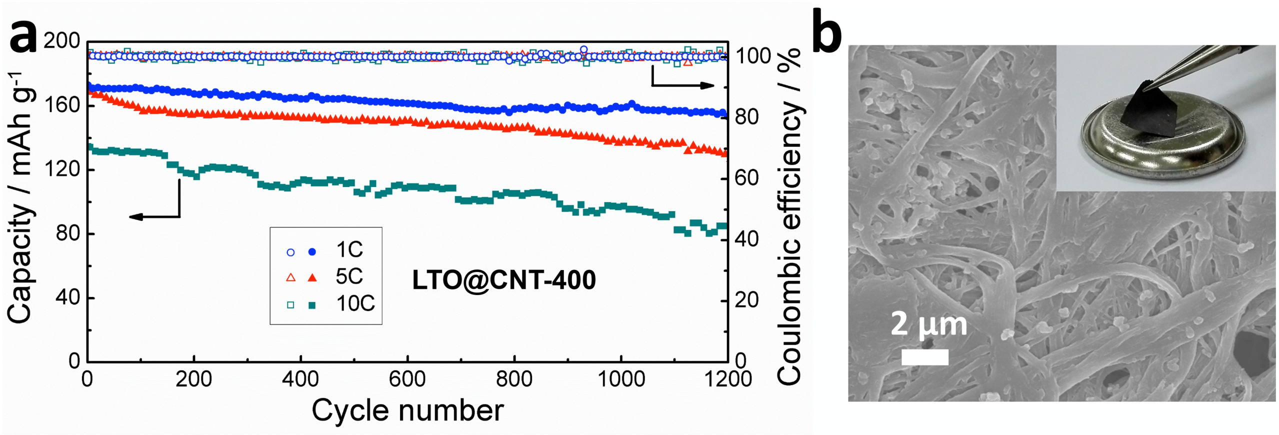

Fig. 6 (a) Long-term cycling behaviors of the LTO@CNT-400 composite at 1C, 2C and 5C. (b) SEM image of the composite after cycling, with an inset of the photograph of the electrode after cycling.